REPORT DOCUMENTATION PAGE

Form Approved OMB NO. 0704-0188

1. REPORT DATE (DD-MM-YYYY)
01-09-2015

2. REPORT TYPE
Final Report

3. DATES COVERED (From - To)
1-Jun-2011 - 31-May-2015

4. TITLE AND SUBTITLE
Final Report: Multifunctional ZnO Nanomaterials for Efficient Energy Conversion and Sensing

5a. CONTRACT NUMBER
W911NF-11-1-0156

5b. GRANT NUMBER

5c. PROGRAM ELEMENT NUMBER
206022

5d. PROJECT NUMBER

5e. TASK NUMBER

5f. WORK UNIT NUMBER

6. AUTHORS
Richard Mu

7. PERFORMING ORGANIZATION NAMES AND ADDRESSES
Fisk University
1000 17th Avenue North

Nashville, TN 37208 -3045

8. PERFORMING ORGANIZATION REPORT NUMBER

9. SPONSORING/MONITORING AGENCY NAME(S) AND ADDRESS (ES)
U.S. Army Research Office
P.O. Box 12211
Research Triangle Park, NC 27709-2211

10. SPONSOR/MONITOR'S ACRONYM(S)
ARO

11. SPONSOR/MONITOR'S REPORT NUMBER(S)
58921-MS-REP.10

12. DISTRIBUTION AVAILIBILITY STATEMENT
Approved for Public Release; Distribution Unlimited

13. SUPPLEMENTARY NOTES
The views, opinions and/or findings contained in this report are those of the author(s) and should not contrued as an official Department of the Army position, policy or decision, unless so designated by other documentation.

14. ABSTRACT
The support has allowed PI- Richard Mu and his team to engaged in a decade of fundamental research in the fabrication, characterization and functionalization of a wide variety of ZnO nanostructures that include nanowires (NWs), nanoscale thin films and quantum well systems to develop novel device and sensor architectures that result in both high emission efficiencies and detection sensitivities.

From an achievement matrix evaluation, ARO/DOD support has generated 35 journal publications, 6 proceeding papers and 2 book chapters in the last 10 years. The program has resulted in 22 awarded master's

15. SUBJECT TERMS
ZnO Nanowires, LED, optical emission, Photoluminescence

16. SECURITY CLASSIFICATION OF:			17. LIMITATION OF ABSTRACT	15. NUMBER OF PAGES	19a. NAME OF RESPONSIBLE PERSON
a. REPORT	b. ABSTRACT	c. THIS PAGE			Richard Mu
UU	UU	UU	UU		19b. TELEPHONE NUMBER 615-329-8507

Report Title

Final Report: Multifunctional ZnO Nanomaterials for Efficient Energy Conversion and Sensing

ABSTRACT

The support has allowed PI- Richard Mu and his team to engaged in a decade of fundamental research in the fabrication, characterization and functionalization of a wide variety of ZnO nanostructures that include nanowires (NWs), nanoscale thin films and quantum well systems to develop novel device and sensor architectures that result in both high emission efficiencies and detection sensitivities.

From an achievement matrix evaluation, ARO/DOD support has generated 35 journal publications, 6 proceeding papers and 2 book chapters in the last 10 years. The program has resulted in 22 awarded master's degrees and 3 PhDs, with all students co-advised by Prof. Mu within the Vanderbilt interdisciplinary materials science program. Currently, there are 3 active PhD, 2 master's, and 1 international exchange PhD student in the group.

From the aspects of fundamental materials research that is relevant to DOD programs, the accumulated knowledge, experience, and infrastructure in reliable and reproducible nanomaterials growth/synthesis with control of nanostructure size, shape, and functionality, in uniform functionalization with both coatings and nanoparticles and in conventional and novel characterization techniques have yielded solid and mature research capabilities that currently include the extensive use of COMSOL Multiphysics simulation and modeling. We are now in a solid position to enter a new and exciting phase of research: materials/structure-by-design (W911NF-12-R-0012-02, Research Area 9: Materials Science; Programs of 9.0; 9.1; and 9.4) More specifically, we would like to utilize the structure-by-design approach to develop high-efficiency optical nanoemitters, such as nano-lasers and nano-LEDs, and ultrasensitive nanoprobes for chemical and biological molecule sensing based on bottom-up design and fabrication of highly complex multifunctional materials with new and unprecedented properties. In addition, we are in the process of developing new analytical techniques capable of characterizing materials at the nanoscale and disentangling the complex behaviors that emerge in highly coupled systems. We are now capable of using COMSOL Multiphysics to model nano- and meso-scale structures to serve as a guide for surface and interface engineering to achieve new and better materials' multifunctionality and capabilities. New analytical methods, in-situ cathodoluminescence (CL) and electron energy loss spectroscopy (EELS) have been developed to characterize the nanoscale structure and energetics and determine the experimental characteristics that will lead to desired material properties at nanometer scales. Thus, the Objectives of the current proposed research are to:

- Fabricate high efficiency optical nanoemitters and biochemical nanoprobes through the combination of computational COMSOL Multiphysics modeling and development of experimental fabrication and characterization techniques – a true structure-by-design method with optimized performance and new functionality,
- Continue to build and expand a comprehensive nanomaterials and sensors research and education program. We have shown that a true successful educational program must emphasize the quality and research-led minority education and training is most effective and sustainable.
- Support and train 1 postdoc, 1 graduate and 1 undergraduate along with two faculty members in ARO/DOD related research. In addition, this proposal will also
- Broaden the reach of ARO/DOD relevant interdisciplinary materials research to the newly founded TIGER Institute at Tennessee State University (5 minutes away from Fisk University).

Enter List of papers submitted or published that acknowledge ARO support from the start of the project to the date of this printing. List the papers, including journal references, in the following categories:

(a) Papers published in peer-reviewed journals (N/A for none)

Received		Paper
09/01/2015	9.00	Daniel C. Mayo, Claire E. Marvinney, Ephraim S. Bililign, James R. McBride, Richard R. Mu, Richard F. Haglund. Surface-plasmon mediated photoluminescence from Ag-coated ZnO/MgO core–shell nanowires, Thin Solid Films, (02 2014): 0. doi: 10.1016/j.tsf.2013.11.131
09/06/2012	2.00	C. Y. Liu, H. Y. Xu, J. G. Ma, X. H. Li, X. T. Zhang, Y. C. Liu, R. Mu. Electrically pumped near-ultraviolet lasing from ZnO/MgO core/shell nanowires, Applied Physics Letters, (08 2011): 63115. doi: 10.1063/1.3625925
09/30/2013	4.00	J. Jones, L. Zhu, N. Tolk, R. Mu. Investigation of ferroelectric properties and structural relaxation dynamics of polyvinylidene fluoride thin film via second harmonic generation, Applied Physics Letters, (08 2013): 72901. doi: 10.1063/1.4817519
09/30/2013	5.00	Daniel C. Mayo, Omari Paul, Idemudia J. Airuoyo, Zhengda Pan, Kenneth E. Schriver, Sergey M. Avanesyan, Hee K. Park, Richard R. Mu, Richard F. Haglund. Resonant infrared matrix-assisted pulsed laser evaporation of TiO2 nanoparticle films, Applied Physics A, (09 2012): 0. doi: 10.1007/s00339-012-7197-7
09/30/2013	6.00	B.J. Lawrie, R. Mu, R. F. Haglund, M. Chergui, A. Taylor, S. Cundiff, R. de Vivie-Riedle, K. Yamagouchi. Ultrafast Surface-Plasmon Enhancement of Exciton and Defect Luminescence in ZnO Thin Films, EPJ Web of Conferences, (03 2013): 0. doi: 10.1051/epjconf/20134104016
09/30/2013	7.00	B. J. Lawrie, R. Mu, R. F. Haglund. Plasmonic Control of Near-Interface Exciton Dynamics in Defect-Rich ZnO Thin Films, Plasmonics, (12 2012): 0. doi: 10.1007/s11468-012-9459-9
09/30/2013	8.00	G. Sekar, R. Akrobetu, R. Mu, S.H. Morgan, Z. Pan. Visible to near-infrared down-conversion luminescence in Tb3+ and Yb3+ co-doped lithium–lanthanum–aluminosilicate oxyfluoride glass and glass-ceramics, Journal of Non-Crystalline Solids, (08 2012): 0. doi: 10.1016/j.jnoncrysol.2012.05.028

TOTAL: 7

Number of Papers published in peer-reviewed journals:

(b) Papers published in non-peer-reviewed journals (N/A for none)

Received		Paper
09/07/2012	3.00	B. J. Lawrie, R. Mu, and R.F. Haglund. Selective Purcell enhancement of defect emission in ZnO thin films, Optics Letters, (05 2012): 1538. doi:
TOTAL:		1

Number of Papers published in non peer-reviewed journals:

(c) Presentations

1. J Hachtel, D Mayo, A Mouti, C Marvinney, R Mu, RF Haglund, A Lupini, “Spatially-Resolved, Three-Dimensional Investigation of Surface Plasmon Resonances in Complex Nanostructures” CLEO: QELS_Fundamental Science, FTh1E. 5 (2015)
2. J Hachtel, A Mouti, D Mayo, C Marvinney, R Mu, R Haglund, S Pennycook, “Probing plasmons in three dimensions in a scanning transmission electron microscope” APS March Meeting Abstracts 1, 8012 (2015)
3. JA Hachtel, D Mayo, A Mouti, C Marvinney, R Mu, RH Haglund, “Cathodoluminescence Imaging of Plasmonic Resorurnances in Ag-Coated ZnO/MgO Core-Shell Nanowires in An Aberation-Corrected Scanning Transmission Electron Microscope”, 8th International Workshop on Zinc Oxide and Related Materials, Sept 7-11 (2014)
4. A Trenchard, D Mayo, J Jones, R Mu, “Time Dependent in-situ Confocal Raman and Optical Emission Investigation of ZnO Nanolayer Films under UV Photon Irradiation”, 8th International Workshop on Zinc Oxide and Related Materials, Sept 7-11 (2014)
5. D Mayo, C MarVinney, J Hachtel, R Mu, R Haglund, “Cavity-Mode Effects on Exciton-Plasmon Coupling in ZnO/MgO Core-Shell Nanowires Decorated by Ag Nanoparticles”, 8th International Workshop on Zinc Oxide and Related Materials, Sept 7-11 (2014).
6. R Mu, H Xu, Y Liu, “Electrically pumped near-ultraviolet lasing from ZnO Nanowire Based Heterojunctions”, APS Meeting Abstracts 1, 50014 (2014).
7. A Trenchard, A Mayo, R Mu, NMSG Team, “ Surface Plasmon-Phonon Interaction in Zinc Oxide and Gold Thin Films”, APS March Meeting Abstracts 1, 1161 (2014)
8. D Mayo, C Marvinney, E Bililign, J McBride, R Mu, R Haglund, “Exciton-Plasmon Coupling in Metal-Nanoparticle-Decorated ZnO/MgO Core-Shell Nanowires”, APS March Meeting Abstracts 1, 1049 (2014)
9. R Mu, A Mayo, H Xu, Y Liu, “Optical and Electrical Characterization of Quantum Dots Decorated ZnO Nanowires for Energy Conversion”, APS Meeting Abstracts 1, 50007 (2014).
10. N Tolk, J Davidson, WP Kang, R Mu, “Room Temperature Deposition Processes Mediated By Ultrafast Photo-Excited Hot Electrons”, VANDERBILT UNIV NASHVILLE TN (2014)

2013

11. C Marvinney, D Mayo, E Bililign, R Mu, R Haglund, “Exciton-Plasmon Coupling in ZnO/MgO Core-Shell Nanowires”, Bulletin of the American Physical Society 58 (2013)

12 A Trenchard, R Mu, “The Effects of Substrates, Buffer and Seeding Layers and Thermal Treatments on Zinc Oxide Nanostructure Formation”, Bulletin of the American Physical Society 58 (2013)

13. S Pak, B Mu, A Mayo, J Jones, R Mu, E Collins, “Fabrication of ZnO Nanostructure Based Polyvinylidene Fluoride Nanocomposites for Energy Application”, Bulletin of the American Physical Society 58 (2013)

14 A Mayo, H Xu, Y Liu, R Mu, "Optical and Electrical Characterization of CdTe Functionalized ZnO Nanowires for Energy”, Bulletin of the American Physical Society 58 (2013)

15. R Mu, “Effects of exciton-plasmon coupling in zinc oxide thin films and nanowires”, Bulletin of the American Physical Society 58 (2013)

16. B Davies, RM Mu, AM Mayo,”Comparative Investigation of TiO2 and ZnO Surface Reactivities for Photovoltaic and Biomedical Applications”, Annual Biomedical Research Conference for Minority Students, B119 (2013)

17. BJ Lawrie, R Mu, RF Haglund, “Ultrafast Surface-Plasmon Enhancement of Exciton and Defect Luminescence in ZnO Thin Films”, BJ Lawrie, R Mu, RF Haglund, EPJ Web of Conferences 41, 04016

2012

18. R. Mu, “Quantum Dots Functionalized Nanostructures for Enhanced Optical Energy. Absorption, Transport and Emission”, BIT Congress Inc., 2nd Annual Nano-S&T-2012, held in Qingdao Kempinski Hotel, China, from October 26-28, 2012

19. D. Mayo, R. Mu, and R. Haglund, “An Investigation of Surface-Plasmon Mediated Emission from Functionalized Zinc Oxide Nanowires Bulletin of the American Physical Society, 79th Annual Meeting of the APS Southeastern Section, Vol 57, Number 16, November 14–17, 2012; Tallahassee, Florida.

Number of Presentations: 19.00

Non Peer-Reviewed Conference Proceeding publications (other than abstracts):

Received	Paper

TOTAL:

Number of Non Peer-Reviewed Conference Proceeding publications (other than abstracts):

Peer-Reviewed Conference Proceeding publications (other than abstracts):

Received	Paper

TOTAL:

Number of Peer-Reviewed Conference Proceeding publications (other than abstracts):

(d) Manuscripts

Received	Paper

TOTAL:

Number of Manuscripts:

Books

Received Book

TOTAL:

Received Book Chapter

TOTAL:

Patents Submitted

Patents Awarded

Awards

Graduate Students

NAME	PERCENT_SUPPORTED	Discipline
Anthony Mayo	1.00	
Andrew Trendchard	1.00	
FTE Equivalent:	**2.00**	
Total Number:	**2**	

Names of Post Doctorates

NAME	PERCENT_SUPPORTED
FTE Equivalent:	
Total Number:	

Names of Faculty Supported

NAME	PERCENT_SUPPORTED	National Academy Member
Richard Mu	0.20	
FTE Equivalent:	**0.20**	
Total Number:	**1**	

Names of Under Graduate students supported

NAME	PERCENT_SUPPORTED
FTE Equivalent:	
Total Number:	

Student Metrics

This section only applies to graduating undergraduates supported by this agreement in this reporting period

The number of undergraduates funded by this agreement who graduated during this period: 4.00

The number of undergraduates funded by this agreement who graduated during this period with a degree in science, mathematics, engineering, or technology fields:...... 4.00

The number of undergraduates funded by your agreement who graduated during this period and will continue to pursue a graduate or Ph.D. degree in science, mathematics, engineering, or technology fields:...... 3.00

Number of graduating undergraduates who achieved a 3.5 GPA to 4.0 (4.0 max scale):...... 4.00

Number of graduating undergraduates funded by a DoD funded Center of Excellence grant for Education, Research and Engineering:...... 0.00

The number of undergraduates funded by your agreement who graduated during this period and intend to work for the Department of Defense 1.00

The number of undergraduates funded by your agreement who graduated during this period and will receive scholarships or fellowships for further studies in science, mathematics, engineering or technology fields:...... 3.00

Names of Personnel receiving masters degrees

NAME	
Andrew Trenchard	
Kenneth Coca	
Total Number:	**2**

Names of personnel receiving PHDs

NAME	
Jennifer Jones	
Total Number:	**1**

Names of other research staff

NAME	PERCENT_SUPPORTED
Anthony Mayo	0.30
FTE Equivalent:	**0.30**
Total Number:	**1**

Sub Contractors (DD882)

Inventions (DD882)

Scientific Progress

See Attachment

Technology Transfer

Highlights ARO/ DOD Support – The Foundation for Structure-by-design

Here we provide a detailed review of the key components that have been accomplished in the past several years under primarily DOD support. They are the cornerstones for the current proposal to develop highly efficient nanoemitters, such as wavelength specific heterojunction nano-LEDs and nano-lasers, and chemical and biological nanosensors with ultrahigh detection sensitivity and low photo and photothermal degradation and damage, such as surface enhanced Raman nanoprobes. The highlights contain three major technical areas: 1) Fabrication Technology for "Structure-by-Design": a) Achieved high-quality and consistent control of ZnO nanowire growth in length, diameter, wire density and uniformity, with growth on various substrate surfaces and b) Developed glancing angle deposition (GLAD) technique to coat ZnO nanowire exterior surfaces with exceptional uniformity and thickness control for ZnO core-shell structures that possess the desirable resonant conditions for a preselected wavelength set (excitation and/or emission wavelengths); 2) New Characterization Techniques have been developed and employed to understand the effects of surface plasmons on the nanostructure, such as enhanced radiative recombination rates due to plasmon-exciton coupling; 3) Recent Progress in COMSOL Multiphysics Modeling to calculate and predict optical field propagation and energy distribution within ZnO core-shell nanostructures to enhance the optical emission for nanoemitters, *i.e.,* nanolasers and nano-LEDs, and to determine Fabry–Perot cavity and/or whispering gallery modes to enhance the sensitivity of bio- and chemical sensors based on the SERS technique.

2.1 Fabrication Technology for "Structure-by-design"

This section contains two key components: ZnO nanowire (NW) growth and the nanowire core-shell fabrication along with the necessary characterization techniques to validate the success of the efforts.

2.1.1 ZnO Nanowire Growth

Motivation: As the need for efficient optoelectronic devices grows, ZnO has emerged as one of the most promising materials for tunable optical emissions. ZnO is a II-VI semiconductor with a wide direct bandgap of 3.37 eV and a large exciton binding energy of 60 meV. This makes the band-edge exciton a more thermally stable near-UV emitter than the commonly used optoelectronic semiconductor GaN, which has a similar bandgap (3.4 eV) but an exciton binding energy of 25 meV. Room temperature photoluminescence (PL) spectra for ZnO show two primary emission bands: a sharply defined band-edge peak centered at 3.37 eV that is a result of exciton recombination, and a broad visible emission peak centered around 2.3 eV that is due to a superposition of donor-acceptor-pair recombinations of near conduction band electrons with deep holes in oxygen vacancies and interstitials.

In the past a few years, the nanomaterials research group at Fisk has established a solid foundation for ZnO nanostructure fabrication with a primary focus on size, shape, and density control. Considerable progress has been made to grow ZnO nanostructures with our custom designed two-zone furnace. We can now routinely grow high-quality, single-crystal ZnO nanostructures with good control of the nanostructure size, shape, length, and orientation, as illustrated in Fig.1. Depending on the nature of the application, one can vary the nanowire growth conditions, employ seeding layers, metal nanoparticle catalysts, use source materials of ZnO + graphite powder or pure Zn, and grow on optically transparent ITO or ZnO thin film conducting layers and other substrates. A number of publications have resulted from this materials fabrication research. [1-7]

2.1.2 Functionalization of ZnO Nanowires for Emission and Sensing Enhancement

By carefully tuning the emission of ZnO nanowires (NWs), a wide variety of high-efficiency devices have been fabricated in recent years, including LEDs[8-10], lasers[11,12], and sensors[13,14]. Although different growth, annealing, and doping conditions have all been employed to control the ZnO emission[15,16], one of the most effective methods for emission enhancement is through coupling to plasmons. Plasmons are the collective oscillations of free electrons relative to fixed positive ion cores in a metal that are driven by the electric field component of incident light. When metal films or nanoparticles are in proximity to a semiconductor, surface plasmon polaritons or localized surface plasmons can be induced that have the potential to drastically enhance or quench emission through coupling of the surface plasmons to the semiconductor luminescent centers.

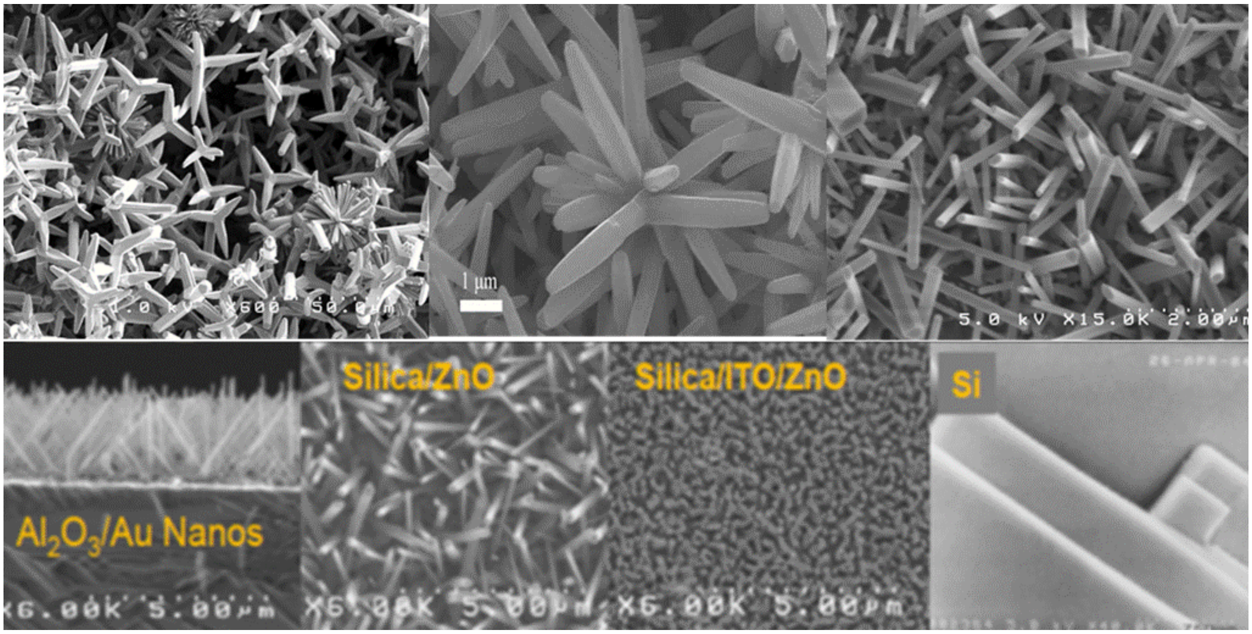

Fig. 1. A set of selected examples of ZnO nanostructures grown in our laboratory on Silica, Si, and other substrates of choice. Some of the ZnO nanowires samples have been used for device fabrication.

The enhancement of ZnO emission due to the presence of Ag nanoparticles can result from a combination of charge transfer and local field effects, which sometimes makes it difficult to resolve the specific mechanisms responsible. Previous research in ZnO thin films separated Ag or Au plasmonic structures from the ZnO using an insulating layer of MgO in varying thicknesses[17]. In this architecture, it was possible to study the effects of near-field exciton-plasmon coupling on the enhancement and quenching of the emission bands and isolate the effects of hot-electron transfer.

In the experiments described here, we followed a similar strategy for NWs, by synthesizing core-shell (ZnO/MgO) NWs and comparing PL yields with and without decorating the NWs with Ag nanoparticles. When ZnO NWs were coated with MgO, the resulting core-shell structure dramatically enhanced the band-edge emission of the ZnO at specific MgO thicknesses. This enhancement is much larger than can be explained by surface passivation of shallow ZnO defects. Instead, we propose that this enhancement is due to optical cavity effects. In addition, once Ag nanoparticles are deposited onto the MgO coating, an even larger band-edge emission enhancement is seen, but the additional enhancement is found to be strongly dependent on MgO shell thickness. This results in a dramatic enhancement that appears to be due to resonant-cavity effects and establishes the plasmonic core-shell nanowire structure as a potentially useful architecture for optoelectronic applications.

ZnO nanowires were grown on the crystalline ZnO seed layer. This step in the growth process utilized a modified vapor-solid method to grow the ZnO NWs onto the ZnO seed layer, using a vertically-oriented tube furnace. The vertically-oriented quartz tube housing used to support the substrate and gas feed lines during deposition is depicted in Figure 1-a. A measured amount (6.0 mg) of Zn powder was placed into a crucible, which was mounted at the bottom of the 0.9 m tall quartz tube housing. The substrate was situated seed layer face-down on two silicon shelves in the substrate holder, and a protective fused silica slide was placed on top of the substrate to prevent unwanted ZnO growth on the back side of the substrate. The substrate was positioned approximately 10 cm above the crucible. Gas feed lines for Ar and O2, a thermocouple, and an exhaust vent, were fed into the growth tube, with the O2 line and thermocouple directly above the substrate, and the Ar line between the substrate and crucible, as indicated in Figure 2-a.

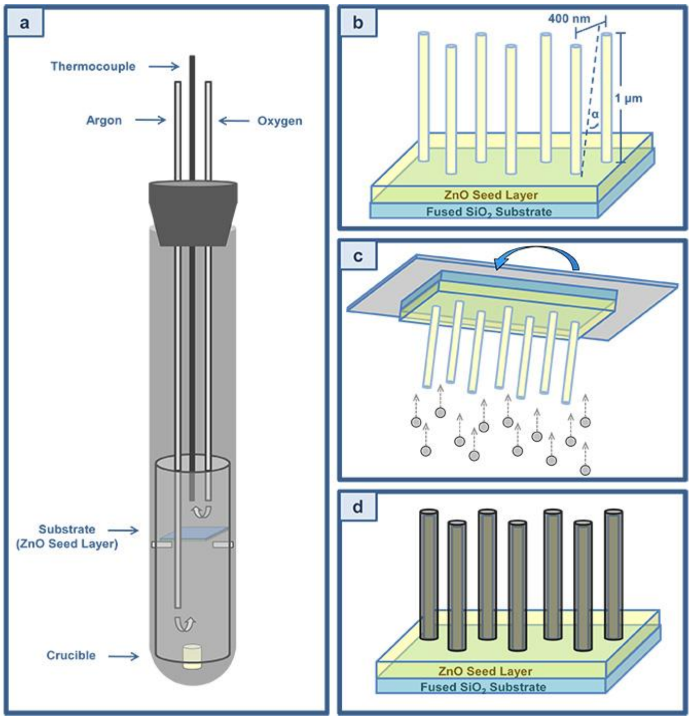

Fig 2 Schematics of (a) vertically oriented quartz tube housing with substrate and gas feed lines, (b) ZnO NW growth on ZnO seed layer and fused silica substrate with measured growth dimensions, (c) the glancing angle deposition (GLAD) process, and (d) coated ZnO NWs after final deposition.

To verify that ZnO NW growth had occurred on the samples, they were viewed by scanning electron microscopy (SEM, Hitachi, S-4200). These images were taken in both the plan view and 45˚ tilt configurations on multiple locations of the sample to gauge the uniformity of the nanowires. The SEM images were analyzed to determine the NW height and interwire spacing of 800 nm and 400 nm respectively. From these measurements the optimal angle needed to coat the nanowires while minimizing shadowing effects was calculated from the inverse tangent of the interwire distance divided by NW height, α = tan-1(1/2) = 27°, as seen in Figure 1-b.

A glancing-angle deposition (GLAD) apparatus was used to continuously rotate the substrate in the electron-beam deposition chamber at the calculated angle, as depicted in Figure 1-c. This resulted in a uniform coating on the NWs, as seen in Figure 1-d. After mounting the ZnO NW sample on the GLAD apparatus, the sample was masked into octants in order to deposit MgO in thicknesses ranging from 0 nm to 70 nm in 10 nm increments, during separate depositions.

Under room temperature and atmospheric pressure conditions, ZnO crystallizes as a hexagonal wurtzite structure. The ZnO NWs grown using the modified vapor-solid method are uniform in thickness, well-aligned, and have hexagonal facets at the ends, as evidenced by SEM imaging of the NWs seen in Figure 3-a, indicative of high quality, single-crystal nanowires. The PL spectra of the bare ZnO NWs in Figure 3-a display a band-edge to visible emission ratio greater than unity, confirming the single-crystal nature of the as-grown ZnO NWs.

Figures 3-b and 3-c display the uniform NW coverage that results from depositing 10 nm of Ag using the GLAD apparatus. The average size of the Ag nanoparticles is approximately 25 nm in diameter, showing 70% coverage uniformly across the surface of the ZnO NWs and the regions between. The uniform deposition was also seen in the MgO spacer layer, with consistent coatings along the sides of the NWs, although a slight thickness variation from the tips to the bases of the NWs is evident, Figure 3-c. The elemental composition of the sample measured by STEM and EDS analysis in Figure 3-c shows distinct regions of Ag, Mg, and Zn, where Mg and Zn represent the locations of MgO and ZnO respectively. The MgO coating not only provides a spacer layer between the ZnO NW and the Ag nanoparticles, but also passivates the surface of the NWs[18-20], which is verified through the quenching of the visible emission in the PL measurements, as seen in Figure 4-a.

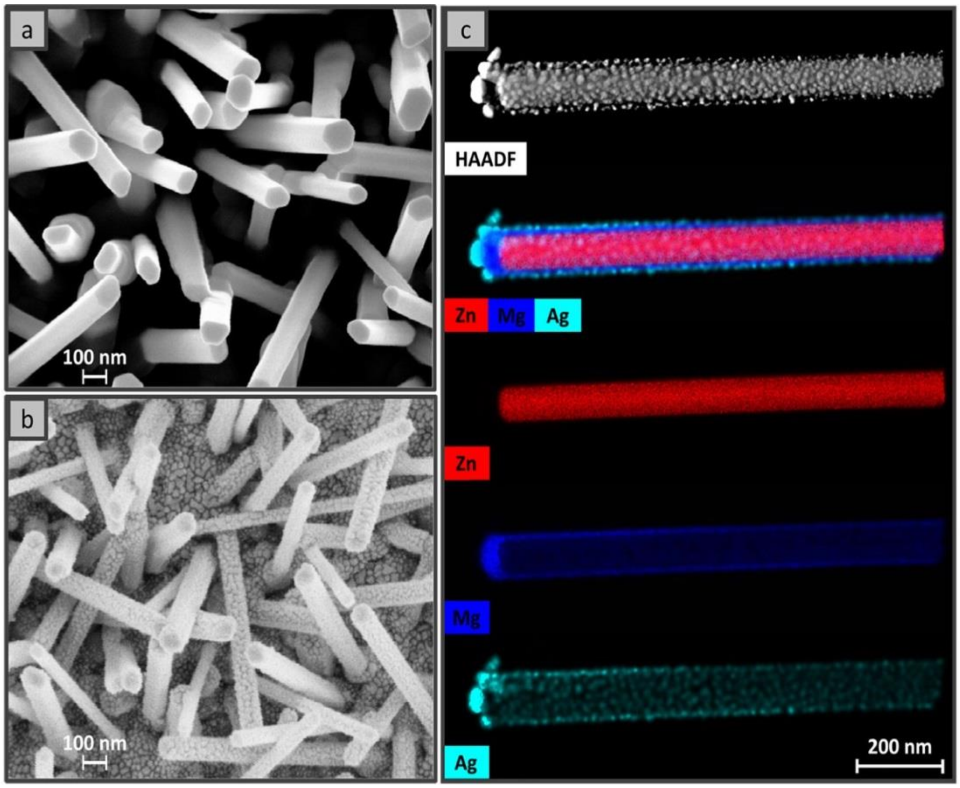

Figure 3. Microscopy of the sample with (a) SEM image of uncoated ZnO NWs, (b) SEM image of Ag coated ZnO NWs, and (c) STEM images of the Ag coated MgO-ZnO core shell NW. From top to bottom: high-angle annular dark-field (HAADF) images from STEM; the energy-dispersive x-ray spectroscopy (EDS) composite; and the EDS of Zn, Mg, and Ag respectively.

Figures 4-a and 4-b show the room-temperature PL spectra of the ZnO nanowires with varying thicknesses of MgO coating and with the core-shell ZnO-MgO structures functionalized with Ag nanoparticles respectively. Insets for Figures 4-a and 4-b display an expanded view of the visible emission spectra. The band-edge and visible emission peaks are located at 379 nm and 497 nm respectively for the ZnO/MgO sample, while the ZnO/MgO/Ag sample peak positions are located at 377 nm and 511 nm. Extinction spectra taken of the samples, not displayed here, show the surface plasmon resonance of the Ag nanoparticles to be centered at 475 nm. The enhancement factors in Figures 4-c and 4-d were calculated from the integrated areas under the emission bands in the PL spectra using a linear baseline and were normalized against the PL spectra from bare ZnO NWs, with and without Ag NPs,, respectively. Both sets of PL spectra show an oscillatory enhancement to the band-edge emission that varies with the thickness of the MgO coating. Maximum enhancement is seen at MgO thicknesses of 20 nm and 60 nm with a minimum at 40 nm. Contrariwise, the visible emission remains relatively constant independent of the MgO thickness.

We propose that the dramatic enhancement of the band-edge emission seen in both ZnO/MgO and ZnO/MgO/Ag structures is primarily due to subwavelength resonant optical cavity modes within the coated nanowires. The optical cavity forms inside a two-dimensional cross section defined by the MgO-ZnO core-shell nanowire and bounded by air as seen in Figure 5-a. At the band-edge emission wavelength of approximately 380 nm, the refractive index of ZnO is approximately 2.45 while that of MgO is approximately 1.77. The reflection at the interface between the oxides due to the difference in refractive indices is modified by the tendency of Mg2+ to diffuse into Zn2+ sites to form Zn1-xMgxO[21,22]. The effective index of the core-shell nanowire structure can be simply calculated as a weighted average. Due to the single-crystal nature of the ZnO nanowires, the faceted surfaces form three degenerate Fabry-Perot cavity modes.

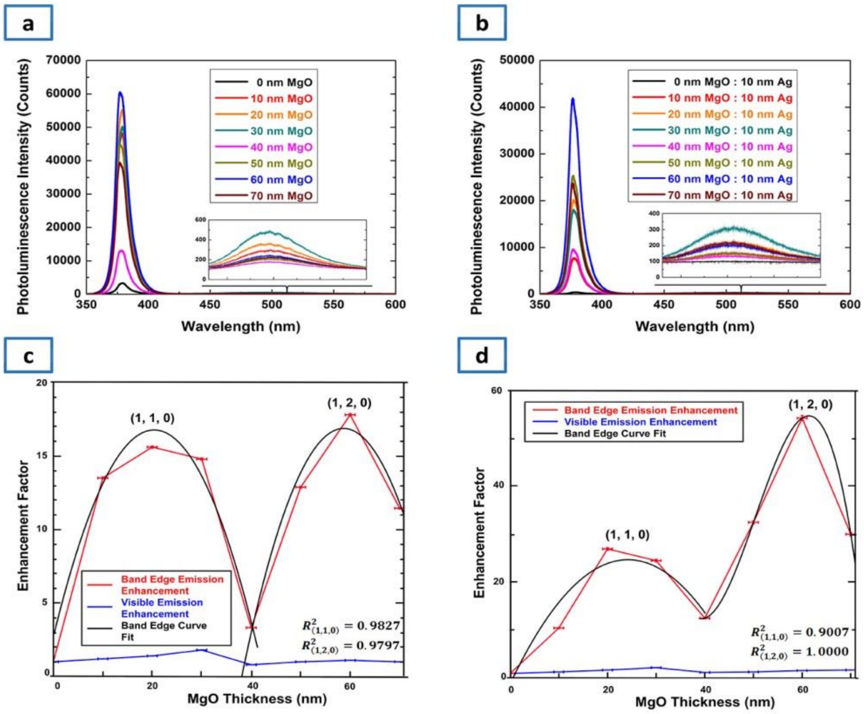

Fig. 4. PL spectra of (a) the MgO/ZnO core-shell NWs and (b) the Ag functionalized MgO/ZnO core-shell NWs, with the inset in both displaying the expanded visible spectra. Enhancement factors in band-edge and visible emission plotted against MgO coating thickness for (c) NWs without Ag nanoparticles, and (d) NWs with 10 nm of Ag nanoparticle coating.

For ZnO NWs of approximately 80 - 90 nm in diameter, Figure 4-b shows the calculated MgO thicknesses for the (1,1,0) and the (1,2,0) modes. The calculations show resonant conditions occurring at thickness values of approximately 20 nm and 60 nm. This is in good agreement with the measured band-edge emission maxima.

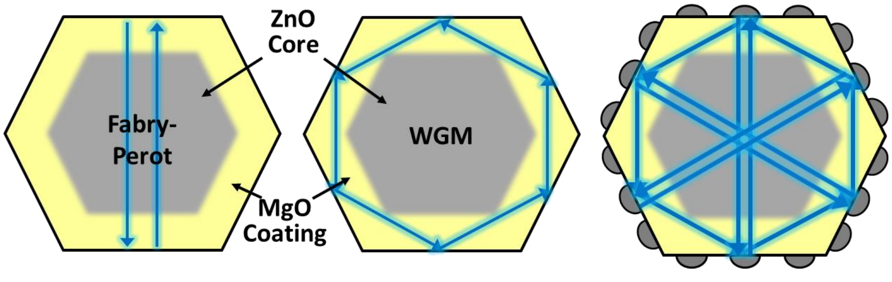

Fig. 5. Two cavity modes present in hexagonal core-shell NWs (lfet & middle), and Ag nanoparticles on core-shell structure surface with cavity mode presence.

Additionally, the visible emission does not show any enhancement over the range of MgO thicknesses. This is also in agreement with the optical cavity explanation since no resonant modes can be excited under this system using ZnO visible emission wavelengths.

Based on the differing shapes and magnitudes of the resonant enhancement for the nanowire structures with and without Ag nanoparticles, we propose the following hypothesis. For the core/shell structures without Ag nanoparticles, the enhanced PL is expected to follow calculated behavior shown in Fig. 4d and the increase in the square-root factor for the (1,2,0) mode is largely compensated by the increased thickness of the MgO shell. For the ZnO/MgO/Ag structures, on the other hand, there is a strong, mode-dependent asymmetry in both magnitude and shape of the PL enhancement. We suggest that the overall increase in enhancement over the ZnO/MgO structures with MgO thickness below 40 nm in the (1,1,0) mode — roughly a factor two — results from Purcell-enhanced radiative recombination rate due to the exciton-plasmon interaction and the enhanced density of states in the localized plasmon resonance. The factor of three enhancement for the ZnO/Mg/Ag nanowires in the (1,2,0) mode, however, is due to the larger spatial extent of the spatially asymmetric (1,2,0) modes compared to the (1,1,0) modes. That greater spatial extent, in turn, increases the exciton-plasmon coupling and thus the Purcell enhancement rate.

Summary 2.1: Reliable fabrication techniques has been estabalished and can produce quality nanostructures from bare ZnO NW growth, core-shell structure, and functionalization of eith bare or core-shell structure with GLAD. We have shown that ZnO-MgO core-shell nanowire structure exhibits optical cavity effects that dramatically enhance the band-edge PL yields in the ultraviolet, while not enhancing visible luminescence. In addition, the plasmonic enhancement of the band-edge emission approximately doubles the PL enhancement due to the resonant cavity effects alone. These results establish the core-shell architecture as an attractive approach to selectively enhance the band-edge emission of ZnO for near-UV optoelectronic applications. Moreover, the core-shell measurements yield interesting insights into the distance dependence of the exciton-plasmon coupling, as the coupling strength reflects the plasmon near-field interaction range. Future work with vertically aligned ZnO NWs grown on templated substrates is expected to yield greater control of the cavity modes and allow for their direct observation by scanning near-field optical microscopy. In addition, Al nanoparticles, which couple more strongly to the band-edge emission of ZnO than Ag[24], can be used to decorate the core-shell structures for additional enhancement.

2.2 Cathodoluminescence and Electron Energy Loss Spectroscopy Study of Metal Nanoparticles on Core-shell ZnO/MgO Nanostructure

This section presents the most recently obtained experimental results. The main boduy of the work has not yet fully published. What we like to demonstrate is that optical techniques, such as photoluminescence, can sample a statistical number of nanostructures with high efficiency. While electron beam methods, such as STEM-CL and EELS, can precisely analyze a single nanowire and a single nanoparticle with high precision. The combination of the two provide an analysis that can paint a thorough picture of the optical behavior of complex plasmonic nanostructures to maximally utilize the plasmonic effects. EELS measures optical properties by detecting excitations caused by the electron beam, while CL measures the subsequent radiative decay. The use of two spectroscopies in tandem within a scanning transmission electron microscope allows to distinguish and perhaps to unravel the plasmonic nature of a randomly shaped and oriented nanoparticle suspended on an insulating/semiconducting nanowires.

Metallic nanoparticles serve many functions in modern nanotechnology[25-28]. One of the most important assets of such nanoparticles is their ability to support surface plasmon resonances (SPRs). SPRs generally have highly-efficient radiative decay, making them useful across multiple optical applications. In photonics, they have been used as nanoantennas to directly absorb and re-emit light[29] or to enhance emission in other optically active materials[30]. In photovoltaics, they are used as a component within solar cells designed to enhance light-absorption efficiency[31]. In all of the applications of SPRs, an understanding of the spatial and spectral locations of the peak intensities within the nanostructure is necessary to maximize the utility of the plasmon.

Here, we have employed CL and EELS in a complementary fashion to probe the plasmonic behavior of nanostructured systems with nanoparticles that are randomly shaped and oriented relative to the beam. By combining the complementary strengths of CL and EELS we can study the plasmonic response in the nanostructure in a rigorous manner in all three dimensions. We examine a silver nanoparticle with an ellipsoid-like morphology suspended on an insulating ZnO/MgO nanowire using both CL and EELS in a scanning transmission electron microscope (STEM) in order to obtain the plasmonic characteristics of the nanoparticle. The crucial element within the experiment is the interplay between CL and EELS. CL is a measure of radiative decay, while EELS is a measure of excitation, meaning the spectrum images gained from each method give different information about the same system. From the combination of CL and EELS we observe three spatially and spectrally distinct plasmon modes within the ellipsoid-like nanoparticle. Due to the differences between the CL and EELS profiles, we can identify them as dipole-like modes in each of the three dimensions and find the spatial locations of their peak intensities. Finally, Fourier-ratio analysis of the low-loss EELS spectrum is used to determine the thickness of the nanoparticle. From the EELS-determined thickness, we roughly know the size of the nanoparticle in all dimensions and see that the variations in the spectral location and intensity of the different plasmonic features are explained through thickness effects. The combination of the CL, EELS,

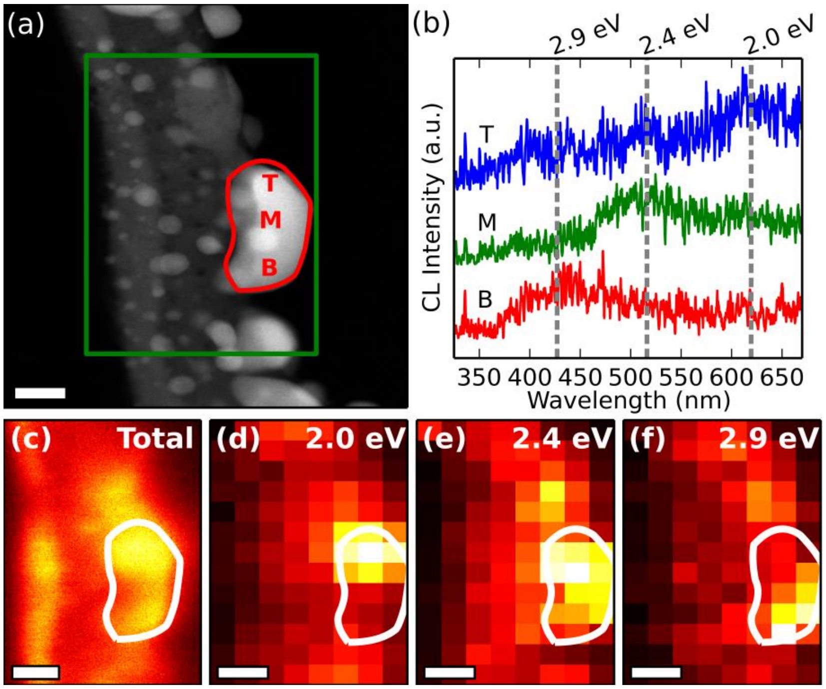

FIG. 6. Cathodoluminescence (CL) on randomly shaped and oriented nanoparticle suspended on an insulating nanowire. (a) Annular dark field (ADF) image of nanostructure and the nanoparticle. The studied nanoparticle is outlined in red. (b) CL spectra taken from three different points, as marked on the in (a). (c-f) The integrated CL intensities in the region of interest marked by the green box in (a) for the total intensity over the entire spectrum (c), and for each of the three distinct CL peaks in (b) at 2.0 eV (d), 2.4 eV (e), and 2.9 eV (f). We see each of these three features is localized to a different part of the nanoparticle, there are no other distinct features from the nanoparticle observed in CL. Scale bar = 50 nm.

and thickness measurements allow us to form a rigorous, complete picture of the plasmonic behavior of the nanoparticle. We focus on the emission spectrum and plasmonic profile of a single large nanoparticle to demonstrate the power of the combination of CL and EELS. An annular dark field (ADF) image of the nanoparticle is shown in Fig. 6a. The nanoparticle has a highly non-symmetric morphology, allowing for non-overlapping plasmonic modes. Additionally, the large size of the nanoparticle helps maximize our signal-to-noise ratio, as well as helping us to spatially distinguish between plasmon modes. The ZnO in nanowire is optically active and a strong emitter, so we select a nanowire with a thick MgO shell (~70 nm) to make sure that the ZnO is insulated from the local field effects of the surface plasmons in the nanoparticle.

In the CL spectrum of the nanoparticle, there are three distinct peaks at three different locations shown in Fig. 6b. We note that at each location the signal is dominated by a different peak in the spectrum. At the top of the nanoparticle (T) we see strong emission centered around 2.0 eV (625 nm), while in the middle (M) we see a weak peak at 2.0 eV and a more dominant peak at 2.4 eV (510 nm). Finally at the bottom (B) the emission comes mainly from a peak at 2.9 eV (425 nm). No peaks are observed above or below this energy range while the probe is on the nanoparticle. To observe the localization of these different peaks we turn to CL. Fig. 6c shows the total luminescent intensity of the nanoparticle (right and highlighted by white outline) and the emitting ZnO nanowire (left). The nanoparticle is shown to emit strongly, even more strongly than the nearby ZnO, but we wish to know the frequency of the collected light as a function of position as well.

To achieve spectral resolution we take a spectrum image (SI). In an SI, a spectrum is collected at each point in a region of interest, marked here by the green square in Figure 1a. Once the SI is obtained we can look at slices, or the integrated intensity of the CL across a 20 nm spectral range centered at the peak of each feature, for each spectrum in the SI to find where that the intensity of that peak is the strongest. Fig. 6d-f shows the SI slices of each of the three peaks shown in Fig. 6b emitting from the nanoparticle. The SI slice spectral widths are 50 nm centered at the peak value. From here we can see that each region of the nanoparticle is dominated by its own feature, with the top of the nanoparticle showing the strongest signal at 2.0 eV, the middle at 2.4 eV and the bottom at 2.9 eV.

Given the localization of these features and the energy range, we classify them as SPRs as Ag is known to have its SPRs in this regime[46]. However, the nature of CL makes a straightforward interpretation of the data intrinsically difficult for a number of reasons. Primarily, in order to get the highly local excitation generated by a 60 kV beam, we sacrifice beam/sample interaction. Thus, in STEM-CL the signal-to-noise ratio and detection efficiency is much weaker than in low-kV CL experiments, which limits the number of spectra that can be acquired without damaging the sample and hence the spatial resolution that can be achieved in a CL SI. Secondly, a parabolic mirror collects *all* light emitted from the sample meaning non-local probe excitations and radiative decay are still counted along with the local signal resulting in a confusion of the origin of the signal. As a result, the type of plasmon mode and the reason for the spatial distribution of the different features we see in the SI slices cannot be determined from CL alone in cases such as ours.

In CL experiments, simulations are widely used to interpret the raw CL data[39,40,47]. However, in most of these experiments colloidal or lithographically patterned nanoparticles which have a well-known morphology are used and can be found in specific orientations which allows for highly accurate simulation of the experimental CL signal. Since we focus on the plasmonic elements (nanoparticles) of complex nanostructures (the nanowires) rather than individual nanoparticles, the exact morphology and orientation of our nanoparticles are not well-known, making simulations difficult. In order to help study our own, as well as other plasmonic nanostructures, we wish to understand the plasmonic CL signal without simulations.

To that aim, we employ low-loss EELS imaging of the same nanoparticle. The comparison of CL and EELS is fruitful for a number of different reasons, all centering on the fact that CL and EELS are complementary to one another. The key difference between the two spectroscopies that causes each to access a different set of optical data is the source of the signal: *EELS probes excitation and CL probes radiative decay*. To elaborate, EELS measures how much energy an electron loses as it passes through the sample, while CL detects the light emitted by the sample after the beam passes through. In other words, EELS tells us how much energy comes into the sample, while CL tells us how much energy comes out in the form of light. The combination of the two allows us to observe the entire lifespan of an optical excitation, from its initial excitation until its return to the ground state.

Now we plot and compare the SIs from EELS to those from CL (Fig. 6) in the optical regime to try and uncover more information about the plasmonic behavior about the nanoparticle. Fig. 7a shows the locations on the nanoparticle from which the representative spectra shown in Fig. 7b are extracted. Four prominent features emerge from the EELS spectra: 2.0 eV, 2.9 eV, 3.6 eV and 3.8 eV. The spatial profiles of each peak are plotted in Fig. 7c-f.

First, we compare the SIs and spectra for the features that appear in both EELS and CL, which are the peaks at 2.0 eV and 2.9 eV. For the 2.0-eV peak in EELS, the signal is localized at the top and bottom of the nanoparticle. By comparing the SI slice for this peak in EELS (Fig. 7c) to the CL slice (Fig. 6d) we gain a sense for the complementary nature of the two spectroscopies. We exploit the higher detection efficiency and spatial resolution of EELS to show us the type of resonance. The localization of the peak at the top and bottom of the nanoparticle in EELS indicates that this peak corresponds to a long-axis surface plasmon. However, the localization of the peak towards the top of the nanoparticle in CL indicates that the mode is more strongly excited at the top of the nanoparticle than at the bottom. Similarly, for the 2.9-eV peak we use the EELS signal to determine the nature of the plasmon mode. The 2.9-eV peak is localized on the left and right side of the nanoparticle, as shown in the EELS SI slice in Fig. 7d, a localization that corresponds to a short-axis SPR. The CL SI slice in Fig. 6e then determines the most active area, which is shown to be the bottom of the nanoparticle. It is important to note that it is not immediately clear why the CL signal is stronger on top for the long-axis mode and stronger on the bottom for the short-axis mode. Once we have discussed the other optical features present in the CL and EELS spectrum we will return to this point and address it more thoroughly.

Now we move onto the optical features that are not present in both the EELS and CL. In Fig. 7e and 7f we see the spatial profiles of two EELS peaks that have no corresponding peaks in CL. The features are at 3.6 eV and 3.8 eV, which correspond to the surface plasmon polaritons (3.6 eV) and the bulk plasmon (3.8 eV)[48]. Looking in the UV range of the CL spectra in Fig. 6b, we see both features are absent. For the case of the polaritons, this highlights one of the key differences between the two types of spectroscopy, namely the difference between imaging radiative decay and imaging excitation. The propagating surface plasmon polaritons are strongly activated within the nanoparticle, but fail to have a strong emission signal due to resistive damping as the polariton propagates between nanoparticles[49,50].

For the bulk plasmons, a strong CL signal is not expected as the plasmon energy are comparable to the thermal energy in a metal, which strongly promotes non-radiative decay[51]. However, even if a signal were present it would not be observable, as the photon detection limit of the CCD in our camera is ~350 nm (the same as the polariton's wavelength), meaning any features further into the UV than that will be invisible to our CL spectrometer. This highlights another important aspect of using both CL and EELS, as CL can only detect photons in the peak absorption range of the CCD, while for EELS the incoming electrons are collected by a scintillator pad coupled with a CCD which allows for electrons of any energy to be detected. Hence, there are some plasmonic features that are visible in EELS, bulk plasmons or surface plasmons with frequencies in the UV and up, that are not visible in CL.

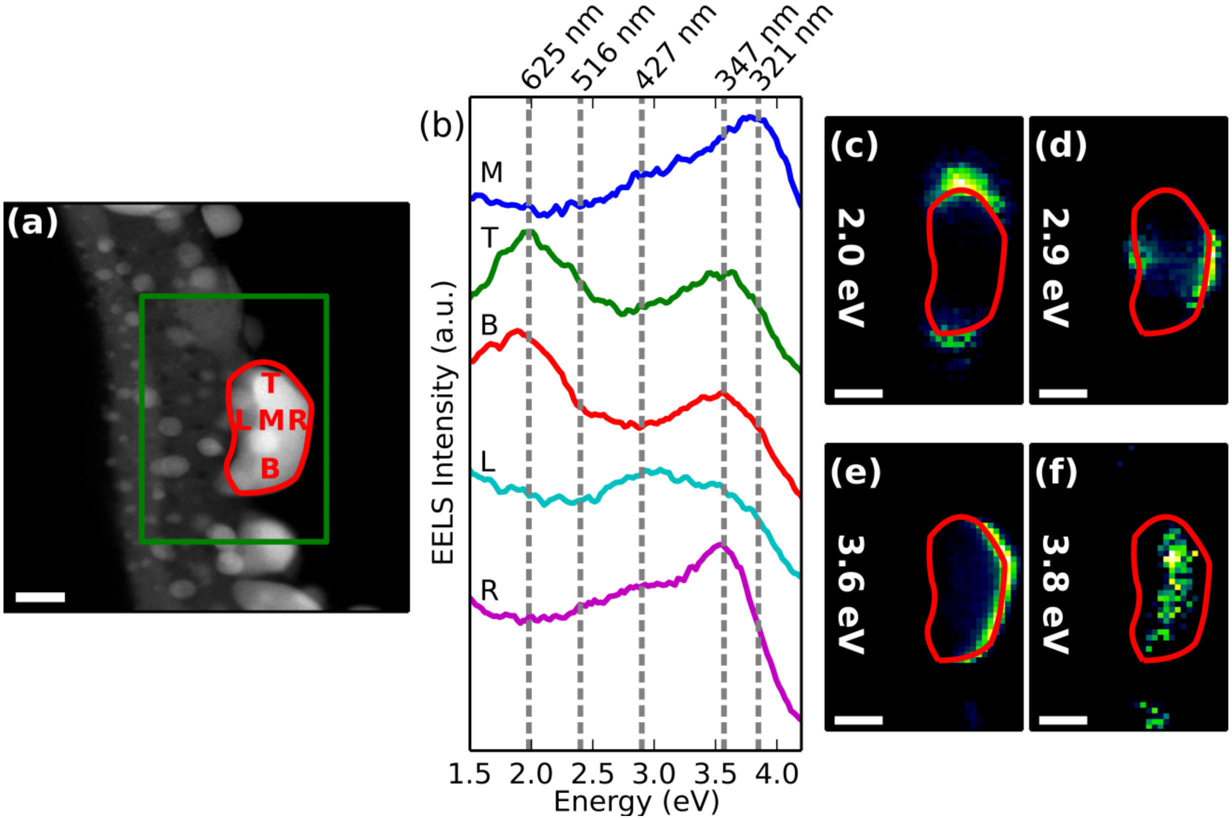

Fig. 7. Electron energy loss spectroscopy (EELS) of nanoparticle in Fig. 6. (a) Annular dark field (ADF) image of nanoparticle, marking locations from which spectra shown in (b) are taken. (b) Representative spectra of the different EELS features. (c-f) Spectrum images showing spatial intensity profiles of the different EELS features, in the region of interest marked by the green box in (a). Some features are present in both CL and EELS, peaks at 2.0 eV (c) and 2.9 eV (d), from the EELS maps we can see that these correspond to long-axis (2.0 eV) and short-axis (2.9 eV) plasmon modes of the ellipsoid-like nanoparticle. Some features are only in EELS, the peaks at 3.6 eV (e) and 3.8 eV (f) were not observed in in CL. From the maps and from literature we know these are the surface plasmon polaritons (3.6 eV) and the bulk plasmon (3.8 eV). Their lack of signal in CL shows that these plasmons decay non-radiatively. Lastly, the 2.4 eV CL peak from Figure 1e is not observed in EELS as can be seen in (b). Presence in CL and not EELS indicates that the peak corresponds to an out-of-plane plasmon localized over the body of the nanoparticle, whose EELS signal is masked by bulk effects. Scale bar = 50 nm.

Finally, we examine the peak that is visible in CL, but has no corresponding EELS feature, namely the peak at 2.4 eV. We see from Fig. 6b and 6e that the peak is a strong feature with its own distinct spatial profile. However, an examination of the EEL spectra in Fig. 7b shows that any EELS intensity at that energy is only a tail of a different peak. Once again we return to the core distinction between EELS and CL, excitation and decay. One of the most important consequences of the distinction is how the signal strengths of the two spectroscopies react to multiple electron-sample interactions. EELS measures excitation by measuring the total energy lost as the electron passes through the sample. As the beam interacts multiple times within the sample, the total energy loss is the sum of the loss of each interaction. Thus, single interactions events are required in order for the measured energy loss to be correct, an effect that is especially important for low-eV features. Examining the different plasmon maps in Fig. 7 we note that the different surface plasmon modes are all observed more strongly along the outside of the particle. The higher contrast along the edge of the nanoparticle is due to the fact that the electron beam can couple to the plasmon's evanescent field and excite the plasmon non-locally[52]. Thus, SPRs excited by the electron beam from the near vicinity of the nanoparticle, but without the beam hitting nanoparticle directly, avoid bulk effects and result in efficient single-interaction excitations and a strong surface plasmon signal. Meanwhile, the body of the nanoparticle only shows a signal from the bulk plasmon. Since electrons passing through the body of the nanoparticle that excite surface plasmons can additionally excite bulk plasmons or interact with the core-electrons, resulting in fewer single-interaction excitations and weaken the surface plasmon signal. Thus, any plasmonic features localized within the body of a thick nanoparticle, are weakly visible or even non-visible in EELS.

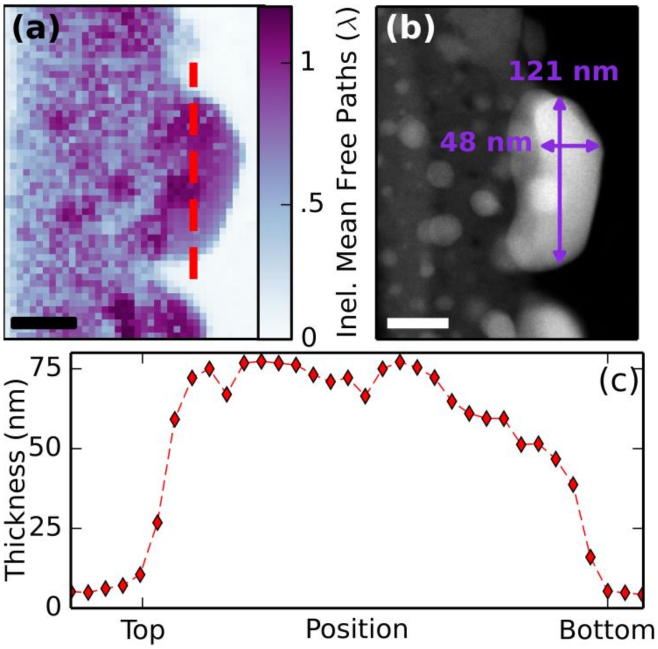

Fig. 8. EELS thickness measurements of nanoparticle. (a) Thickness map of nanoparticle/nanowire assembly, in terms of the inelastic mean free path. The thickness at the bottom of the nanoparticle differs significantly from the top. (b) ADF image with the measured width (~50 nm) and length (~120 nm) of the nanoparticle. (c) A line profile of the absolute thickness of the nanoparticle, through the red line in (a). The nanoparticle has two sections, the top ~75 nm thick, and the bottom ~50 nm thick. The region of the nanoparticle that is 75 nm approximately correlates to the region of the nanoparticle emitting at 2.4 eV seen in FIG. 1e, showing that the 2.4 eV out-of-plane plasmon mode corresponds to a thickness of 75 nm. Additionally the thickness profile explains the localization CL signals for the long-axis plasmon (2.0 eV) at the top of the nanoparticle and the short-axis (2.9 eV) at the bottom. The long-axis plasmon is localized at the top, because the nanoparticle is thicker there, and hence there is higher beam/sample interaction which is proportional to CL signal. At the bottom both the width and the thickness are at 50 nm increasing the efficiency of exciting plasmons corresponding to that thickness. Scale bar = 50 nm.

CL does not lose signal strength in the case of multiple interactions, as each interaction is an excitation that eventually must return to the ground state via recombination or radiative decay. More excitations translates to more radiative decay and stronger CL signal. So while an electron that passes through the body of a nanoparticle activates both the surface and bulk plasmons, the surface plasmons radiatively decay at their own unique frequency, and are hence efficiently collected regardless of multiple interactions. Thus, the optical feature at 2.4 eV is likely a surface plasmon that is localized over the body of the nanoparticle, since it has a distinct peak in CL, but none in EELS. Out-of-plane, longitudinal plasmon modes have been shown to be strongly active in CL studies[40-42] indicating that the 2.4 eV signal is a longitudinal plasmon mode, oscillating in the beam direction. Thus we have used the combination of CL and EELS to image and measure longitudinal plasmon modes in all three dimensions.

Finally, we return to the point mentioned earlier concerning why the CL signal for the long-axis plasmon is localized at the top of the nanoparticle, and the short-axis plasmon is localized at the bottom. To address this point we take advantage of another aspect of low-loss EELS, and utilize Fourier-ratio deconvolution techniques to measure the thickness of the nanoparticle[53]. The thickness of the nanowire/nanoparticle assembly in terms of inelastic mean free path lengths (λ), is shown in Fig. 8a. We see that at the base of the nanoparticle, the thickness of the nanoparticle decreases significantly from ~1 λ to ~0.7 λ. We recall from Fig. 6 that the CL signal varied significantly in the same region, indicating that thickness and morphology effects likely play an important role. Hence, measure the width and length of the nanoparticle from the ADF Image in Fig. 8c to be ~120 nm and ~50 nm respectively. Then we use the STEM acquisition settings and the atomic weight of Ag to determine an absolute thickness, measured in nm, of a line profile of the nanoparticle (the red line in Fig. 8a, plotted in Fig. 8c). From this we see that the nanoparticle has two principal regions; a thick region at the top that is ~75 nm thick, and a thinner region at the bottom that is ~50 nm thick.

We can now use all three maps, CL, EELS, and EELS-thickness, to explain the complete three-dimensional plasmonic behavior of the nanoparticle. There are three principal localized surface plasmon resonances, as we can see from the CL SI, resonances at 2.0 eV, 2.4 eV, and 2.9 eV. From the EEL SI, we can determine that the 2.0-eV and 2.9-eV resonances correspond to the long-axis and short-axis plasmon modes of the ellipsoid-like nanoparticle, as well as easily excited polariton and bulk plasmons that we know to not be optically active from the CL. The absence of the 2.4 eV-peak in EELS combined with its presence in CL tells us the peak is a plasmon mode localized over the body of the nanoparticle, namely an out-of-plane plasmon mode. The emission at this unique energy spatially corresponds to the same region of the nanoparticle that has the unique thickness of ~75 nm. Finally, the EELS-thickness explains the CL intensity variances of the long-axis and short-axis plasmon modes. For the long-axis mode, the CL signal is localized towards the top of the nanoparticle, the thickest region. Since this plasmon mode operates perpendicularly to the beam direction the increased thickness means higher beam/plasmon interaction, hence more excitation and radiative decay. Then for the short-axis plasmon mode, localized at the bottom of the NP in CL, both the thickness and the width of the nanoparticle in the peak CL intensity region is ~50 nm. Hence, the short-axis and out-of-plane plasmon modes are at the same frequency, increasing the total cross section of plasmon emission at this energy value.

In **Summary 2.2:** we combine STEM-CL and STEM-EELS to identify the dominant plasmon modes in a randomly shaped and oriented nanoparticle and determine the type of mode and the spatial profile of its intensity without the use of simulations. CL and EELS alone leave gaps in our understanding of the plasmons, as CL cannot detect plasmons that do not decay radiatively and suffers from relatively poor spatial resolution, while EELS is highly sensitive to thickness and bulk effects which only allows for efficient study at the edges of the nanoparticle or in thin structures. The combination of CL and EELS has no such blind spot as the weaknesses of one technique are the strengths of the other, and allow for a rigorous, three-dimensional understanding of the plasmonic behavior of metallic nanoparticles regardless of size, shape, or orientation.

2.3 Preliminary Results of COMSOL Multiphysics Modeling and Its Perspectives

During the last year or so, efforts have been made to use COMSOL multiphysics to model optical cavity effects and compare with our previous experimental results optical enhancements of ZnO core-shell structure as a function initial ZnO NW diameter and MgO layer thickness as the shell. Nice agreements have been obtained and Fig, 11 is a good example. COMSOL Multiphysics is used to compute the cavity modes for specific shell thicknesses and elucidate the mechanisms underlying increased enhancement of the radiative emission rate for the higher-order modes. Simulations show that the cavity modes include a strongly confined Fabry-Perot resonance as the lowest-order mode and higher-order whispering-gallery modes that lead to an enhanced field intensity near the surface of the core-shell nanowire (Fig. 3c). Since the photoluminescence yield depends on the coupling strength between the ZnO excitons and the localized silver plasmons, the closer spatial proximity of the higher-order modes to the Ag nanoparticles results in an enhanced radiative emission rate due to the Purcell mechanism.

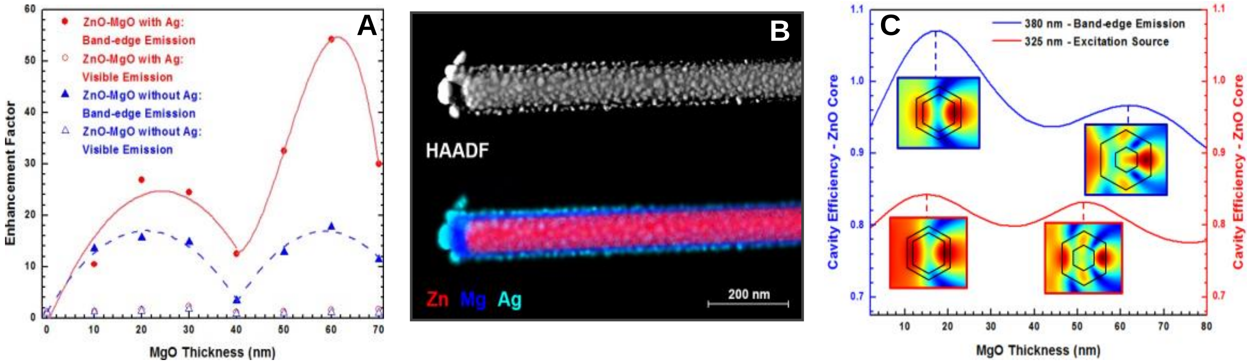

Fig. 11: Fabricated ZnO NWs core-shell structure and their optical and structure anaysis. A) Photoluminescence enhancement *vs* MgO shell thickness. Red and blue data points correspond to ZnO-MgO core-shell structures with and without Ag, respectively. B) Scanning transmission electron micrograph of single nanowire (top) showing Zn core (red), Mg shell (blue) and Ag nanoparticles (aqua). C) COMSOL simulations of optical cavity efficiencies for both 380 nm (band-edge emission) and 325 nm (excitation source).

Bibliography

1. D. C. Mayo, C. E. Marvinneya, E. S. Bililignb, R. Mu, R. F. Haglund Jr. “Surface-plasmon mediated photoluminescence from Ag-coated ZnO-MgO core-shell nanowires”, Thin Solid Films 553, 132 (2014)
2. R.S. Aga Jr, D. Gunther,A. Ueda, Z. Pan, W.E. Collins, R. Mu and K. Singer, “Hybrid Solar Cell Based on ZnO Nanowires Decorated with CdTe Quantum Dots”, Nanotechnology 20 465204 (2009).
3. R. Aga, Jr., A. Ueda, Z. Pan, W.E. Collins, and R. Mu, K. Singer, J. Shen, “Enhanced Photoresponse in Decorated ZnO Nanowires with CdTe Quantum Dot”, Appl Phys Lett 91, 212308 (2007)

4. E. Jackson, E. Aga Jr, A. Steigerwald, A. Ueda, D. Coffey, L. Allard, Z. Pan, W.E. Collins, R. Mu, "Characterization of CdTe nanoparticles fabricated by pulsed electron deposition technique at different parameters", Physica Status Solidi C 3, 3582 (2006)
5. T.K. Francis, A. Ueda, R. Aga Jr, Z. Pan, W. E, Collins, and R. Mu, "Annealing effects on the photoluminescence and morphology of ZnO nanowires" Physica Status Solidi C 3, 3573 (2006)
6. Y. H. Tong, Y. C. Liu, C. L. Shao, and R. Mu, "Structural and Optical Properties of ZnO Nanotower Bundles", Appl. Phys. Lett 88, 123111 (2006)
7. S. Chen, Y.C. Liu, C. Shao, R. Mu, *et al.* "Structural and Optical Properties of Uniform ZnO Nanosheets", Adv. Mat. 17, 586 (2005)
8. M. Young Bae, K. Whon Min, J. Yoon, G.-T. Kim, J. Sook Ha, Journal of Applied Physics 113/8 (2013) 084310.
9. X. Chen, A.M.C. Ng, A.B. Djurišić, W.K. Chan, P.W.K. Fong, H.F. Lui, C. Surya, C.C.W. Cheng, W.M. Kwok, Thin Solid Films 527 (2013) 303.
10. G. Li, A. Sundararajan, A. Mouti, Y.J. Chang, A.R. Lupini, S.J. Pennycook, D.R. Strachan, B.S. Guiton, Nanoscale 5/6 (2013) 2259.
11. C.-S. Wang, H.-Y. Lin, J.-M. Lin, Y.-F. Chen, Applied Physics Express 5/6 (2012) 062003.
12. X.Y. Liu, C.X. Shan, S.P. Wang, Z.Z. Zhang, D.Z. Shen, Nanoscale 4/9 (2012) 2843.
13. J.J. Hassan, M.A. Mahdi, C.W. Chin, H. Abu-Hassan, Z. Hassan, Sensors and Actuators B: Chemical 176 (2013) 360.
14. C.W. Na, H.S. Woo, I.D. Kim, J.H. Lee, Chemical communications 47/18 (2011) 5148.
15. M. Jung, S. Kim, S. Ju, Optical Materials 33/3 (2011) 280.
16. L. Sun, H. He, C. Liu, Z. Ye, Journal of Applied Physics 108/12 (2010) 124313.
17. R.F. Haglund, Jr., B.J. Lawrie, R. Mu, Thin Solid Films 518/16 (2010) 4637.
18. Y. Wu, W. Wu, X.M. Zou, L. Xu, J.C. Li, Materials Letters 84 (2012) 147.
19. H.Y. Yang, S.F. Yu, G.P. Li, T. Wu, Opt. Express 18/13 (2010) 13647.
20. J. Li, D. Zhao, X. Meng, Z. Zhang, J. Zhang, D. Shen, Y. Lu, X. Fan, The Journal of Physical Chemistry B 110/30 (2006) 14685.
21. Q. Jiang, H. Zheng, J. Wang, H. Long, G. Fang, ACS applied materials & interfaces 4/12 (2012) 7043.
22. M. Xue, Q. Guo, K. Wu, J. Guo, Langmuir 24/16 (2008) 8760.
23. C. Jin, H. Kim, H.-Y. Ryu, H.W. Kim, C. Lee, The Journal of Physical Chemistry C 115/17 (2011) 8513.
24. B.J. Lawrie, K.W. Kim, D.P. Norton, R.F. Haglund, Jr., Nano Lett 12/12 (2012) 6152.
25. Anker, J. N. et al. Biosensing with plasmonic nanosensors. Nat. Mater. 7, 442–453 (2008).
26. Mirkin, C. A., Letsinger, R. L., Mucic, R. C. & Storhoff, J. J. A DNA-based method for rationally assembling nanoparticles into macroscopic materials. Nature 382, 607–609 (1996).
27. Kamat, P. V. Photophysical, Photochemical and Photocatalytic Aspects of Metal Nanoparticles. J. Phys. Chem. B 106, 7729–7744 (2002).
28. Maier, S. A. et al. Local detection of electromagnetic energy transport below the diffraction limit in metal nanoparticle plasmon waveguides. Nat. Mater. 2, 229–232 (2003).
29. Novotny, L. & van Hulst, N. Antennas for light. Nat. Photonics 5, 83–90 (2011).
30. Mayo, D. C. et al. Surface-plasmon mediated photoluminescence from Ag-coated ZnO/MgO core–shell nanowires. Thin Solid Films 553, 132–137 (2014).

31. Ferry, V. E., Munday, J. N. & Atwater, H. A. Design Considerations for Plasmonic Photovoltaics. Adv. Mater. 22, 4794–4808 (2010).
32. Yamamoto, N., Araya, K. & García de Abajo, F. J. Photon emission from silver particles induced by a high-energy electron beam. Phys. Rev. B 64, 205419 (2001).
33. Willets, K. A. Probing local electromagnetic field enhancements on the surface of plasmonic nanoparticles. Prog. Surf. Sci. 87, 209–220 (2012).
34. Kociak, M. & Stéphan, O. Mapping plasmons at the nanometer scale in an electron microscope. Chem. Soc. Rev. 43, 3865–3883 (2014).
35. Kociak, M. et al. Seeing and measuring in colours: Electron microscopy and spectroscopies applied to nano-optics. Comptes Rendus Phys. 15, 158–175 (2014).
36. Nelayah, J. et al. Mapping surface plasmons on a single metallic nanoparticle. Nat. Phys. 3, 348–353 (2007).
37. Bosman, M., Keast, V. J., Watanabe, M., Maaroof, A. I. & Cortie, M. B. Mapping surface plasmons at the nanometre scale with an electron beam. Nanotechnology 18, 165505 (2007).
38. Mazzucco, S. et al. Ultralocal Modification of Surface Plasmons Properties in Silver Nanocubes. Nano Lett 12, 1288–1294 (2012).
39. Myroshnychenko, V. et al. Plasmon Spectroscopy and Imaging of Individual Gold Nanodecahedra: A Combined Optical Microscopy, Cathodoluminescence, and Electron Energy-Loss Spectroscopy Study. Nano Lett. 12, 4172–4180 (2012).
40. Coenen, T., Bernal Arango, F., Femius Koenderink, A. & Polman, A. Directional emission from a single plasmonic scatterer. Nat. Commun. 5, (2014).
41. Coenen, T., Vesseur, E. J. R., Polman, A. & Koenderink, A. F. Directional Emission from Plasmonic Yagi–Uda Antennas Probed by Angle-Resolved Cathodoluminescence Spectroscopy. Nano Lett. 11, 3779–3784 (2011).
42. Zhu, X. L. et al. Confined Three-Dimensional Plasmon Modes inside a Ring-Shaped Nanocavity on a Silver Film Imaged by Cathodoluminescence Microscopy. Phys. Rev. Lett. 105, 127402 (2010).
43. Sherry, L. J. et al. Localized Surface Plasmon Resonance Spectroscopy of Single Silver Nanocubes. Nano Lett. 5, 2034–2038 (2005).
44. Kumar, A., Fung, K.-H., Mabon, J. C., Chow, E. & Fang, N. X. Excitation and imaging of resonant optical modes of Au triangular nanoantennas using cathodoluminescence spectroscopy. J. Vac. Sci. Technol. B 28, C6C21–C6C25 (2010).
45. Nicoletti, O. et al. Three-dimensional imaging of localized surface plasmon resonances of metal nanoparticles. Nature 502, 80–84 (2013).
46. Hao, E. & Schatz, G. C. Electromagnetic fields around silver nanoparticles and dimers. J. Chem. Phys. 120, 357–366 (2004).
47. Gómez-Medina, R., Yamamoto, N., Nakano, M. & Abajo, F. J. G. de. Mapping plasmons in nanoantennas via cathodoluminescence. New J. Phys. 10, 105009 (2008).
48. Rocca, M. Low-energy EELS investigation of surface electronic excitations on metals. Surf. Sci. Rep. 22, 1–71 (1995).
49. Maier, S. A. & Atwater, H. A. Plasmonics: Localization and guiding of electromagnetic energy in metal/dielectric structures. J. Appl. Phys. 98, 011101 (2005).
50. Sweatlock, L. A., Maier, S. A., Atwater, H. A., Penninkhof, J. J. & Polman, A. Highly confined electromagnetic fields in arrays of strongly coupled Ag nanoparticles. Phys. Rev. B 71, 235408 (2005).
51. Fox, Mark. Optical Properties of Solids. (Oxford University Press, 2010).

52. Chu, M.-W. et al. Probing Bright and Dark Surface-Plasmon Modes in Individual and Coupled Noble Metal Nanoparticles Using an Electron Beam. Nano Lett. 9, 399–404 (2009).
53. Egerton, R. F., Wang, F., Malac, M., Moreno, M. S. & Hofer, F. Fourier-ratio deconvolution and its Bayesian equivalent. Micron 39, 642–647 (2008).
54. Kim, J., Lee, G. J., Park, I. & Lee, Y. P. Finite-Difference Time-Domain Numerical Simulation Study on the Optical Properties of Silver Nanocomposites. J. Nanosci. Nanotechnol. 12, 5527–5531 (2012).
55. C. Y. Liu, H.Y. Xu, J. Ma, X.H. Li, X.T. Zhang, Y.C. Liu and R. Mu, "Electrically pumped near-ultraviolet lasing from ZnO/MgO core/shell nanowires", Appl Phys Lett 99, 063115 (2011)
56. W. Z. Liu, H. Y. Xu, L. X. Zhang, C. Zhang, J. G. Ma, J. N. Wang and Y. C. Liu, Appl. Phys. Lett., 2012, 101, 142101.
57. W. Z. Liu, H.Y. Xu, C.L. Wang, L.X. Zhang, C. Zhang, S.Y. Sun, J. G. Ma, X. T. Zhang, J. N. Wang, and Y.C. Liu, Nanoscale, 2013, 5, 8634–8639